metals

MDPI

Article

The Engine Casing Machining Holes Repairing Based on Vibration Wire Feeding

Yunlong Pan [1], Sheng Gao [1], Haichao Li [2,*], Wentao Zhang [2] and Yixuan Ma [2]

[1] School of Mechanical Science and Engineering, Northeast Petroleum University, Daqing 163318, China; panyllong@sina.com (Y.P.); gaosheng_china@126.com (S.G.)
[2] State Key Laboratory of Advanced Welding and Joining, Harbin Institute of Technology, Harbin 150001, China; 22s009158@stu.hit.edu.cn (W.Z.); mayixuan_hit@stu.hit.edu.cn (Y.M.)
* Correspondence: lihaichao@hit.edu.cn

Abstract: The engine casing components operate in high-temperature and high-pressure environments. Process holes are drilled when defects occur. Welding is employed in the repair of process holes as a process for permanently joining materials. The traditional welding method relies on padding, which results in poor back formation of process holes. Additionally, the shape of the process holes imposes high requirements on the size of the droplet transition. The conventional approach of adjusting a welding current makes it difficult to achieve stable droplet transition and precise formation of small holes. It poses a challenge for the robotic welding process. To deal with this problem, the influence of the high-frequency vibration GTAW process on the directional transition of molten droplets is studied. The molten droplet directional transition process is developed. The impact of vibration energy on the molten pool is reduced. Welding repair experiments for process holes are successfully conducted. When the frequency is 3 Hz, the transition of droplets changes from a continuous one-droplet transition to a discontinuous liquid bridge transition. The residual height and mechanical properties of the repaired area are tested. The experimental results indicated that the residual height after dual-side repair is $\leq$0.7 mm. The X-ray and fluorescent penetration tests have a 100% first-pass qualification rate. The repaired area demonstrates a hardness of 480 HV and a room-temperature tensile strength of 1069 MPa. The repair process requirements for the casing are met.

Keywords: aerospace casing; additive repair; TC4 (titanium alloy); industrial robots; intelligent manufacturing

check for updates

Citation: Pan, Y.; Gao, S.; Li, H.; Zhang, W.; Ma, Y. The Engine Casing Machining Holes Repairing Based on Vibration Wire Feeding. *Metals* **2024**, *14*, 319. https://doi.org/10.3390/met14030319

Academic Editor: Michael Rethmeier

Received: 18 January 2024
Revised: 1 March 2024
Accepted: 6 March 2024
Published: 11 March 2024

Copyright: © 2024 by the authors. Licensee MDPI, Basel, Switzerland. This article is an open access article distributed under the terms and conditions of the Creative Commons Attribution (CC BY) license (https://creativecommons.org/licenses/by/4.0/).

1. Introduction

The aircraft casing, known as the engine's "skeleton", serves as its primary load-bearing part. With its large size, intricate structure, thin walls, and high precision requirements, it necessitates advanced precision casting techniques [1]. Surface defects are inevitable during the casting of titanium alloy casings, leading to the formation of casting process holes. To remedy these issues, manual gas tungsten inert gas welding (GTAW) is typically employed for repairs [2]. The casing plays a vital role in ensuring their smooth and prolonged operation as the core component of aircraft engines. There is a stringent requirement for precision in repairing aircraft casings [3]. However, traditional manual GTAW for repairs makes it challenging to ensure the forming quality of the non-machined areas on the backside of the blades. This limitation significantly affects the casing's performance [4,5].

At present, the main techniques for additive repair include HVOF (High-Velocity Oxygen Fuel), PASW (Plasma Arc Surfacing Welding), laser cladding, arc additive manufacturing, GTAW overlay welding, etc. [6–10]. The repair process is categorized into two methods: spraying and cladding, and the repair materials can be divided into powder and wire.

Spraying is a process that involves physical bonding, with most of the released heat coming from the impact of the powder and the substrate. The heat generated has minimal impact on the substrate [11,12]. On the other hand, traditional GTAW cladding has a higher heat input. The released heat significantly affects the crystal orientation and grain size of the substrate [13–15]. Spraying lacks metal element diffusion and penetration between weld materials and substrates as a physical bonding process. It leads to lower bonding strength and poor impact resistance. It is mechanically inferior to the cladding process.

This study on aircraft engine repair was conducted using HVAF in 2023 [16]. A deposition layer with a porosity less than 2, a maximum hardness of 380 ± 20 HV, and a wear rate of about 10^{-4} mm^3/Nm was prepared. However, its mechanical properties are significantly lower than those obtained by other repair methods. The spray coating does not involve diffusion and penetration of metal elements between the welding material and the base material as a physical bonding process, resulting in lower bonding strength and poor impact resistance. It makes the mechanical properties far inferior to those achieved by welding processes.

Powder is commonly used in the spraying process, while wire is more prevalent in cladding. With the emergence of laser technology, processing powder with laser melting reduces heat input impact on the substrate while ensuring weld material and substrate bonding [15–18]. However, laser-sprayed deposition layers may still exhibit internal pores and a lack of fusion, with lower density and mechanical properties compared to wire. It makes them susceptible to chunky detachment.

In 2021, a pre-melting electron beam additive manufacturing method was used to prepare Ti-6Al-4V titanium alloy [19]. The tensile strength was increased from 784 MPa to 840 MPa compared to traditional electron beam wire deposition, and the longitudinal height variation on the deposited surface was within ≤0.2 mm. A study on the mechanical properties of SLM-additive Ti-6Al-4V parts was conducted, as well as the microstructure within small holes and the lack of correlation between fusion domains [20]. The research revealed that when the porosity is ≤6%, the samples maintained yield strength and UTS values, but there was a slight loss in elongation. However, as the defect density increased, the elongation decreased.

These methods are mostly utilized for repairing surface wear, cracks, and surface modifications. However, there is limited research on repairing through-hole defects and controlling the forming processes of both the front and back sides. The challenge in repairing through-hole defects lies in the inability to process the backside after repair. The focus is on controlling the transition of molten droplets to ensure the quality of the backside forming, aiming to meet the performance requirements of the repaired component [21].

In 2022, the influence of heat input on the microstructure and mechanical properties of the deposited Ti-6Al-4V alloy was investigated [22]. The study found that high heat input (10^6 J/m) resulted in columnar grains exhibiting significant anisotropic tensile strength. Low heat input (5×10^5 J/m) transformed columnar grains into equiaxed grains. The rapid cooling rate during solidification at a lower heat input (1600–1660 °C) led to a larger proportion of equiaxed grains, significantly reducing tensile strength anisotropy. At temperatures below 700–1006 °C, the high heat input produced a large amount of nitrogen, α' martensite, and fine secondary α, with tangled dislocations during the secondary α phase transformation. This resulted in greater tensile strength and hardness compared to low heat input. The weld seam morphology, defects, mechanical properties, and microstructure of deposits obtained by Electron Beam Melting (EBM), Tungsten Inert Gas (TIG), and Laser Beam Welding (LBW) of Ti-6Al-4V were compared [23,24]. The results revealed that internal defects in EBM Ti-6Al-4V samples produced during the manufacturing process were smaller than those occurring during the welding process. In TIG welding, large voids were distributed along the edges of the weld seam, while in laser welding, they were distributed on top of the weld seam. The center grain size of LBW welds was much smaller than that of TIG welds. TIG-welded samples had more heat at the boundaries of the weld seam. The mechanical properties of TIG-welded components were superior

to those of laser-welded components, primarily due to the larger cross-sectional area of the weld seam compared to the center. Additionally, a microstructure examination of TIG welding revealed fewer defects in the weld seam than LBW. Moreover, the elongation rate of all samples was very low.

The full-process control of the welding repair process is achieved by employing low-frequency vibration wire feeding in conjunction with the high-frequency GTAW process to control the directed transition of molten droplets. This approach fulfills the requirement of single-side welding with dual-side forming, enabling controllable shaping of the backside. Additionally, an automated robot system is developed with the capabilities of automatic recognition and path planning for repairing small holes in casings. The welding repair is conducted successfully on cast process holes in aircraft casings. Automated welding repairs for process holes in the engine casing have been achieved.

2. Experiments

2.1. Experiments System

The experimental system, as shown in Figure 1, consists of a six-degree-of-freedom industrial robot, a TIG inverter DC welding power source, a dynamic wire feeding system, a visual inspection system, a welding workstation, and a self-developed automatic wire feeding argon arc welding gun device. The directed transition of molten droplets is achieved by adjusting the wire feeding frequency of the dynamic wire feeding system and the current of the TIG inverter DC welding power source. Additionally, the visual inspection system detects the position and aperture of the repair area. It automatically plans the repair path with the aid of process parameters stored in the database.

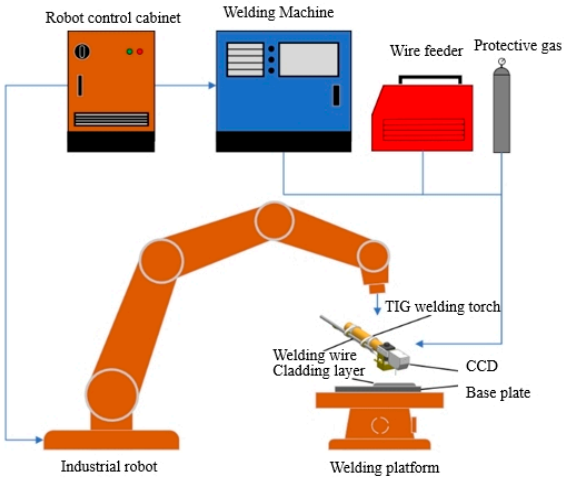


Figure 1. The overall framework of system.

The clear droplet contours were recorded during the preliminary experimental stage using a pool monitoring camera in the dynamic wire feeding system to better observe the influence of vibrational wire feeding on the directed transition of droplets. The TigSpeed dynamic wire feeding system (German EWM company, Mündersbach, Germany) adds a reciprocating motion to the continuous wire feeding process. This high-frequency linear vibration is applied along the direction of the wire. While achieving automatic wire feeding, the high-frequency reciprocating motion of the wire feeder imparts an additional transitional force to the wire. This facilitates the active detachment of molten droplets from the wire, promoting their transition into the molten pool. Through analysis of the collected dynamic images, patterns of the impact of vibrational wire feeding on droplet transition were obtained.

The experimental base material chosen is cast ZTC4 titanium alloy with a thickness ranging from 2 mm to 4.5 mm. The chemical composition of this material is detailed in Table 1. For the repair material, TC4 titanium alloy welding wires with diameters of

Φ1.0 mm and Φ1.2 mm are selected. The chemical composition of these repair wires is presented in Table 2.

Table 1. Chemical composition of ZTC4 titanium alloy (%, mass fraction).

Al	V	Fe	Si	C	N	H	O	Ti
5.5~6.8	3.5~4.5	≤0.40	≤0.15	≤0.10	≤0.05	≤0.015	≤0.25	Bal

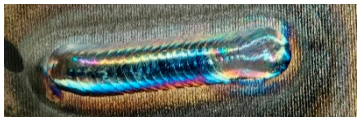
Table 2. Chemical composition of TC4 wire (%, mass fraction).

Al	V	Fe	C	N	H	O	Ti
5.5~6.3	3.6~4.4	≤0.25	≤0.05	≤0.05	≤0.015	≤0.20	Bal

2.2. Additive Repair Experiments

To ensure the quality of the back formation in the automatic repair of through-hole defects, the key is to address the stability of the "hanging plug welding" process. Initially, an orthogonal experiment was conducted based on Table 3 to investigate the influence of different process parameters on deposition formation. A comparison revealed that, with the same deposition speed, the width of the deposition layer gradually increased with the increase in current. The deposition layer was narrowest at a welding current of 75 A and widest at a welding current of 90 A. Similarly, with the same current, an increase in deposition speed led to a gradual narrowing of the deposition layer. The deposition layer was widest at a deposition speed of 40 mm/min and narrowest at a deposition speed of 70 mm/min, with a decrease in the forming quality of the deposition layer.

Table 3. The orthogonal experiments of the deposition parameters.

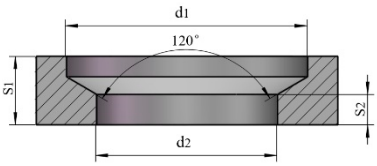
No.	Current (A)	Deposition Speed (mm/min)	Welding Speed (m/min)	Wire Diameter (mm)	The Deposition Image
1	75	40	0.3	1.0	
2	80	40	0.3	1.0	
3	90	40	0.3	1.0	
4	75	60	0.3	1.0	
5	75	70	0.3	1.0	

The welding current is 75 A, the wire feeding speed is 0.3 m/min, and the deposition speed is 40 mm/min for the deposition process based on the requirements for the

performance of titanium alloy aerospace engine casings and considering the results of the orthogonal experiment. Additionally, a reasonable deposition path is planned to ensure the stability of the deposition repair experiments.

The experiments are conducted on the repair-forming processes for holes with diameters of Φ4 mm, Φ6 mm, Φ8 mm, Φ10 mm, and Φ12 mm based on the welding characteristics of titanium alloy materials and the requirements for casing repair, which are shown in Table 4. Different thicknesses, top hole diameters, and chamfer heights are designed based on varying repair hole diameters for GTAW additive repair process experimentation.

Table 4. Test items and parameters.

No.	Aperture d1 (mm)	Process Hole d2 (mm)	Thickness s2 (mm)	Root Face s1 (mm)	Groove Feature Design
1	4	7	2	1~1.3	
2	6	10	3	1~1.3	
3	8	12	4	1.8~2	
4	10	16	4.5	2	
5	12	16	4.5	2	

3. Result

3.1. Molten Droplet Transition Behavior and Mechanical Model

The descent of the droplet is influenced by various forces, including gravity (G), surface tension F_σ, plasma flow force F_a, electromagnetic force F_{em}, and mechanical force F generated by wire vibration during deposition combining the analysis from droplet transition dynamics theory. When the summation of forces $\sum F$ is greater than the surface tension force F_σ as per Equation (1), droplet transition into the weld pool occurs.

During the directional transition of the molten pool, the gravitational force G of the molten droplet, the mechanical force F generated by wire vibration feeding, the plasma flow force Fa, and the electromagnetic force F_{em} act as promoting forces for the directional transition of the molten droplet. The magnitude of the mechanical force F generated by wire vibration feeding is related to parameters such as wire feeding speed and vibration frequency. In Equations (1)–(5), θ represents the wire feeding angle, ε represents the groove angle, r_d represents the radius of the molten droplet, ρ represents the density of the molten droplet, g represents the gravitational acceleration, A represents the amplitude, f represents the vibration frequency, t represents time, v_f represents the plasma velocity, ρ_f represents the density of the plasma fluid, C_d represents the drag coefficient, μ_0 represents the magnetic permeability of vibration, I represents the welding current, and r_w represents the electrode radius.

Surface tension F_σ acts as a hindering force for the directional transition of the molten droplet. In Equation (5), R represents the radius of the welding wire, and σ represents the surface tension coefficient. By introducing mechanical force F into the transition of the molten droplet and controlling the amplitude A and vibration frequency f, the size of the molten droplet's radius r_d can be effectively reduced, thereby reducing the hindrance of surface tension on the transition of the molten droplet. This achieves control over the directional transition of the molten droplet.

$$\begin{gathered} \sum F = (cos\theta + cos(\varepsilon - 90^\circ - \theta))F + (tan\theta + \tfrac{1}{cos(\varepsilon - 90^\circ)})G + F_{em} + F_a > F_\sigma \\ (with\ \varepsilon \neq 0) \\ \sum F = (cos\theta - cos(90^\circ + \theta))F + tan\theta G + F_{em} + F_a > F_\sigma \\ (with\ \varepsilon = 0) \end{gathered} \quad (1)$$

$$G = \frac{4}{3}\pi r_d^3 \rho g \tag{2}$$

$$F = \frac{4}{3}\pi r_d^3 \rho A (2\pi f)^2 \sin(2\pi f + \pi) \tag{3}$$

$$F_a = 0.5\pi v_f^2 \rho_f r_d^2 C_d \tag{4}$$

$$F_{em} = \frac{\mu_0 I^2}{4\pi}\left[ln\frac{r_{d\sin\theta}}{r_W} - \frac{1}{4} - \frac{1}{1-\cos\theta} + \frac{2}{(1-\cos\theta)^2} ln\frac{2}{1+\cos\theta}\right] \tag{5}$$

$$F_\sigma = 2\pi R\sigma \tag{6}$$

The influence of different vibration frequencies on the molten droplet transition during through-hole defect repair is shown in Figure 2. The results showed transition times of 560 ms at f = 0 Hz, 960 ms at f = 1 Hz, and 280 ms at f = 3 Hz. Morphological analysis of the deposited layers under different frequencies (shown in Figure 2g) indicated that at f = 0 Hz, the weld bead width was notably larger compared to f = 3 Hz. Additionally, f = 1 Hz exhibited the widest bead width but lower surface quality compared to f = 0 Hz and f = 3 Hz in terms of surface formation. As the frequency of wire vibration feeding continues to increase, there is no significant change in the surface-forming quality.

At a vibration frequency of f = 0 Hz (as shown in Figure 2a), the volume of the wire end droplet continuously increases as the arc melts the welding wire. The droplet transition takes the stable form of a continuous transition limited by surface tension.

At a vibration frequency of f = 1 Hz (as shown in Figure 2b), it is noted that the wire end droplet still transitions in the form of a large-volume droplet. However, due to the vibration of the welding wire, the droplet transition time is significantly longer than at f = 0 Hz, and the droplet volume is also significantly larger than at f = 0 Hz.

With an increased vibration frequency of f = 3 Hz (as shown in Figure 2c), the droplet transition changes from the original large-volume droplet transition to a liquid bridge transition. The droplet transition process is stable. As the deposition time increases, the droplet transition evolves from a continuous liquid bridge transition to a discontinuous liquid bridge transition. It reduces the effect of vibration energy on the molten pool.

Observations of the droplet transition process in Figure 2d reveal that when the vibration frequency f is 10 Hz, the mode of droplet transition is essentially the same as when f = 3 Hz, but the volume of the droplet at the wire end is smaller. However, the process of the wire being withdrawn from the molten pool becomes unstable. From 2212 ms to 2304 ms, the droplet transition still occurs intermittently as a discontinuous liquid bridge transition, while from 2305 ms to 2313 ms, it transitions to a continuous liquid bridge. The simultaneous presence of continuous and discontinuous liquid bridge transitions greatly increases the risk of wire vibration feeding causing agitation in the molten pool.

Observations of the droplet transition process in Figure 2e reveal that as the vibration frequency increases to f = 12 Hz, with a further increase in the vibration frequency of wire feeding, the melting process at the wire end shifts from edge melting by the arc during mid-frequency vibration to central melting by the arc. The volume of the droplet at the wire end increases due to receiving more energy, resulting in larger droplets. However, unlike at f = 1 Hz, due to the high-frequency vibration, the droplets are rapidly fed into the molten pool and quickly withdrawn from it. The droplet transition process does not exhibit the issue of oversized droplets observed at f = 1 Hz, and the transition mode remains one droplet at a time.

Observations of the droplet transition process in Figure 2f reveal that when the vibration frequency is f = 16 Hz, due to the excessively high frequency, the wire end does not undergo a melting process. Instead, the welding wire is directly fed into the molten pool, where it is melted by the energy in the molten pool. The welding wire is then quickly withdrawn from the molten pool, still resulting in intermittent liquid bridge transitions.

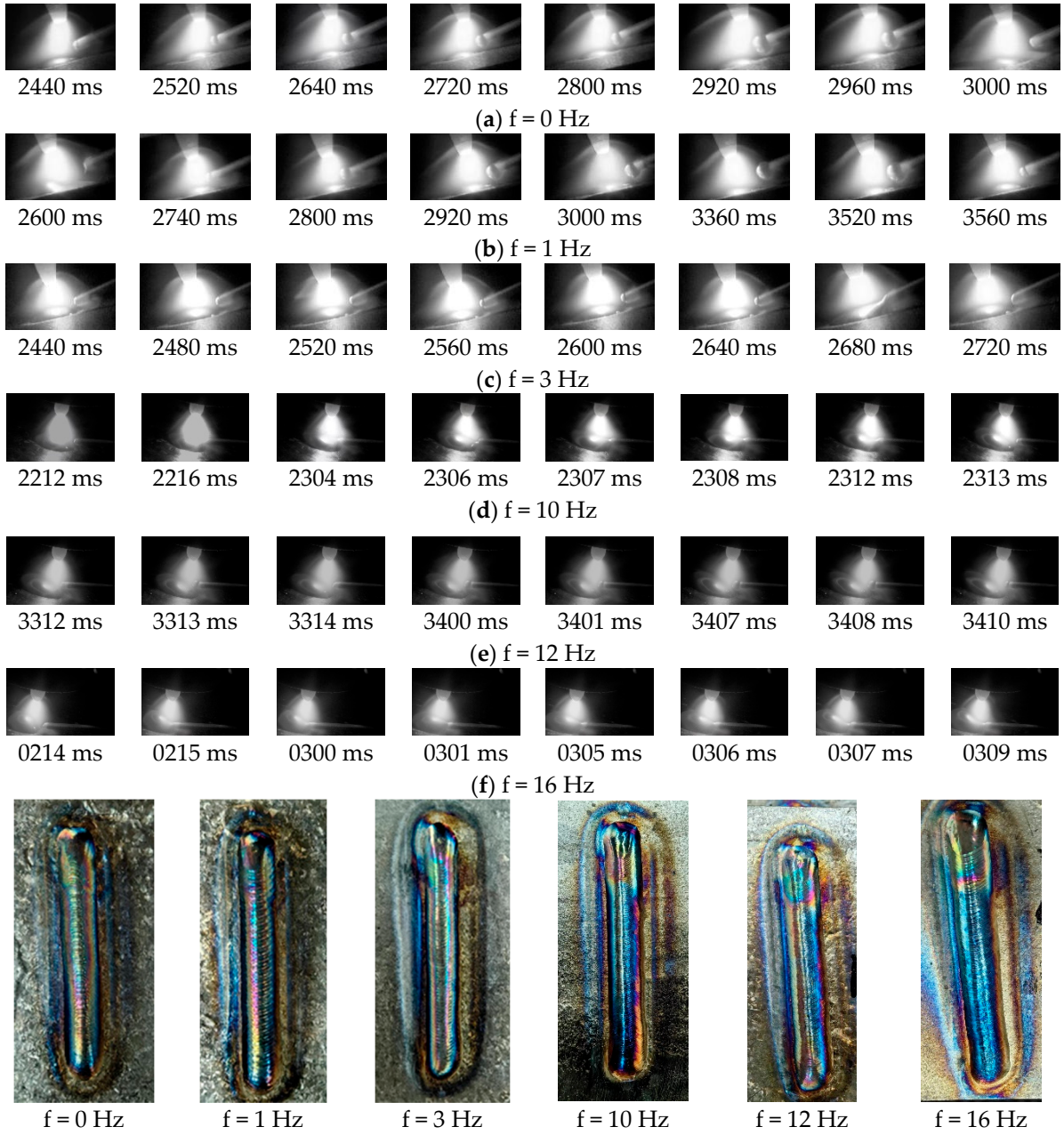


Figure 2. Surface formation under different wire feeding frequencies.

Through comparative analysis of the droplet detachment behavior at different frequencies of wire vibration feeding, it is found that when f = 1 Hz, the droplet transition is unstable. At f = 10 Hz, the occurrence of both continuous and intermittent liquid bridge transitions can disrupt the stability of the molten pool, posing a risk of deposition layer misalignment. At f = 12 Hz, alternating central and edge melting occurs at the wire end, making it difficult to effectively control the droplet detachment behavior. When the vibration frequency reaches f = 16 Hz, the welding wire is directly fed into the molten pool for end melting, which is not conducive to the repair process studied in this research. When the vibration frequency is set to f = 3 Hz, the droplet transition achieves the most stable intermittent liquid bridge transition. Therefore, this study selects f = 3 Hz as the vibration frequency for subsequent experiments.

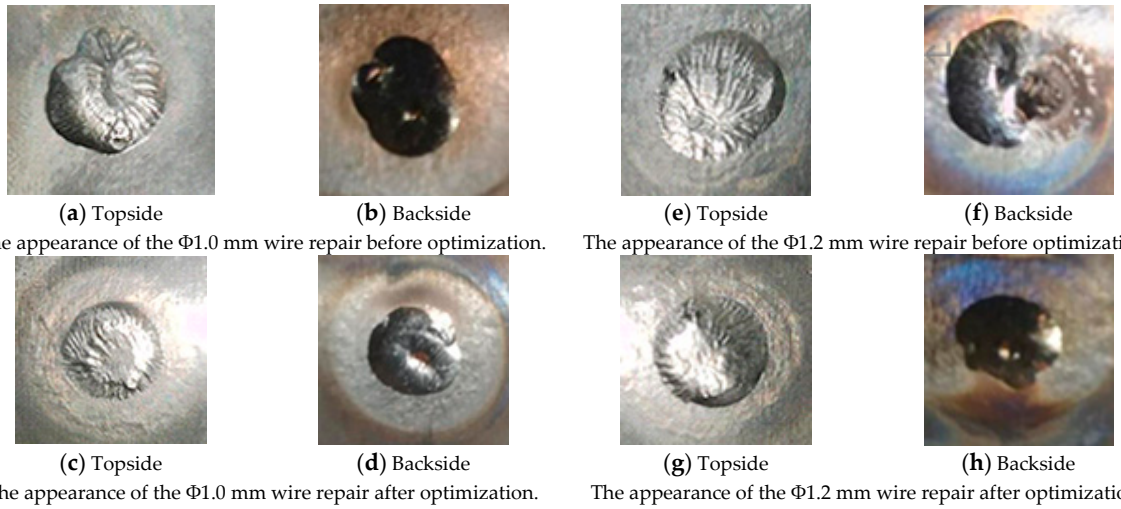
The molten droplet transition occurs steadily with a continuous volume increase when the vibration frequency is 0 Hz. The transition is constrained due to surface tension,

appearing as a stable and consistent droplet-by-droplet process. The molten droplet transition resembles droplets with a relatively larger volume when the vibration frequency is 1 Hz. However, the droplet transition time is notably longer than f = 0 Hz due to wire vibration causing the wire end to move away from the arc region.

The droplet transition changes from large-volume droplet transitions to liquid bridge transitions when the vibration frequency is 3 Hz. This transition remains stable, but prolonged deposition time shifts the continuous liquid bridge transition to intermittent. It reduces the impact of vibration energy on the weld pool.

In the low-frequency auxiliary wire feeding repair process, the surface tension of the molten droplet remains constant. Compared to traditional wire feeding methods, the droplet is influenced by axial forces along the wire during the transition process. This facilitates control over the droplet size and transition direction, leading to a reduced droplet volume. The droplet transition changes from a coarse droplet transition to a continuous liquid bridge transition and then to a intermittent liquid bridge transition.

The 3 Hz frequency for the vibrating wire feeding repair process aids rapid droplet transition, preventing wire sticking and ensuring shaping quality (as shown in Figure 3). However, when using Φ1.0 mm wire for repairs, the softness of the titanium alloy wire leads to intermittent instability during wire feeding. There is a collapse at the repair center. The formation quality of the repair cannot be guaranteed. (as shown in Figure 3a,b).



(**a**) Topside (**b**) Backside (**e**) Topside (**f**) Backside

The appearance of the Φ1.0 mm wire repair before optimization. The appearance of the Φ1.2 mm wire repair before optimization.

(**c**) Topside (**d**) Backside (**g**) Topside (**h**) Backside

The appearance of the Φ1.0 mm wire repair after optimization. The appearance of the Φ1.2 mm wire repair after optimization.

Figure 3. The diameter of the welding wire is relative to Φ4 mm forming effect.

The Φ1.2 mm wire significantly enhances repair quality (as shown in Figure 3e,f), but the back formation height is difficult to control due to the larger wire diameter. More heat input is required to melt the wire, resulting in an increased demand for heat input during the repair process. This leads to a reduction in the control of droplet transition behavior during the repair process. Optimizing wire length and structure resulted in a stable wire feeding mechanism. The Φ1.0 mm wire has the best repair performance. Figure 3c,d depict optimized Φ4 mm hole repair after enhancement.

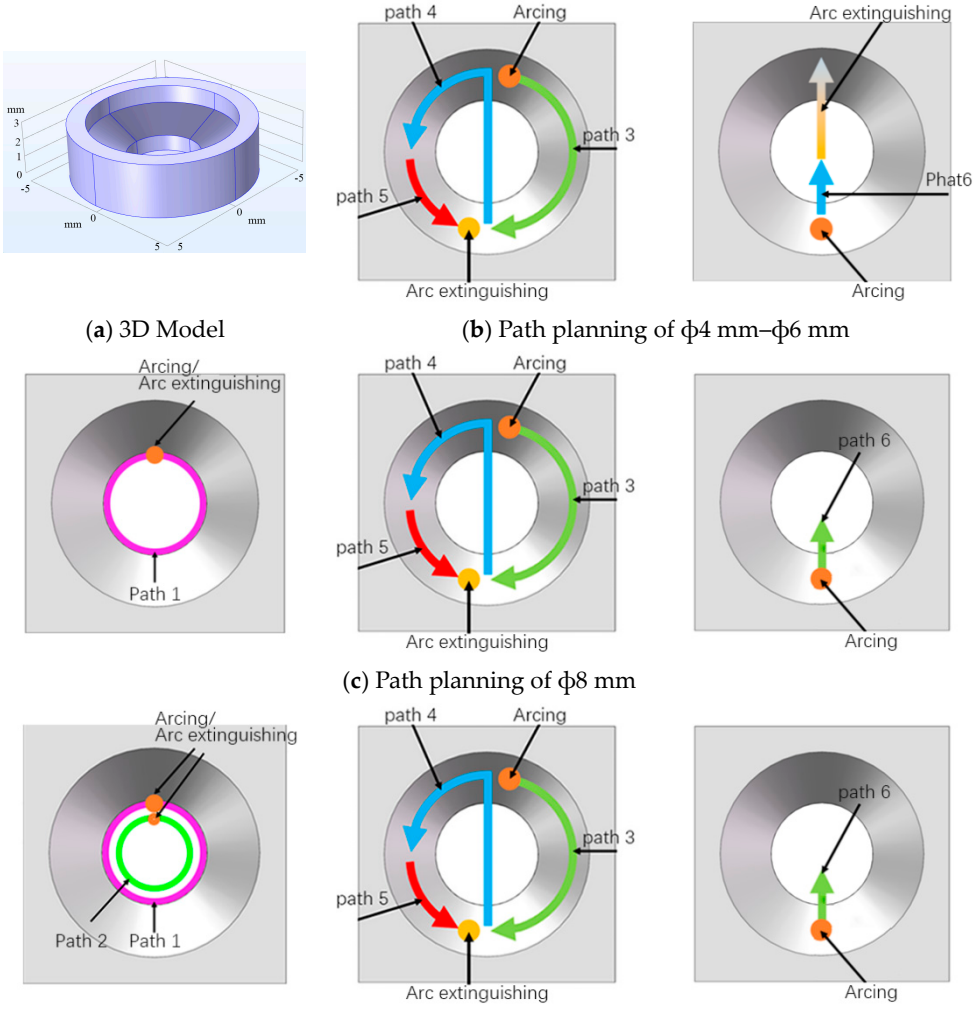
3.2. Influence of Droplet Transfer Trajectory on the Formation of Process Holes

Through research on repairing forming with different apertures, it has been found that the repair-forming process is extremely sensitive to the welding heat input when repairing titanium alloy plates of different thicknesses. If the heat input is insufficient, there is a high risk of incomplete penetration on the backside. Conversely, excessive heat input is likely to result in a burn-through or melt-through.

Through research on the directional transition repair-forming characteristics of TC4 material droplets, the scale of the aperture is divided into three stages. When the aperture is between φ4 mm and φ6 mm, direct repair of small holes is feasible. For apertures ranging

from φ8 mm to φ10 mm, it is necessary to first perform a diameter reduction repair on the base hole. When the aperture is ≥φ10 mm, multiple layers and multiple passes of diameter reduction repair are required for the base hole.

We utilized a controllable heat source, as depicted in Figures 4b and 5, to perform segmented repairs on small holes. By controlling the partitioned heat input, it is possible to maintain the temperature of the repair area in a relatively stable state. As shown in Figure 4c,d, when the repair aperture is ≥φ8 mm, it is necessary to first fill the base hole to reduce its diameter. This helps avoid excessive residual height or even burn-through on the backside caused by excessive heat input during the repair process.



(**a**) 3D Model (**b**) Path planning of ϕ4 mm–ϕ6 mm

(**c**) Path planning of ϕ8 mm

(**d**) Path planning ofϕ10 mm–ϕ12 mm

Figure 4. Repair path planning for different apertures.

In Figure 4b, path 3 represents the first segment of the repair path, where the thermal input is relatively high to ensure that the repair area quickly reaches the deposition temperature, thus avoiding repair defects due to insufficient temperature. Path 4 represents the second segment of the repair path. In this stage of deposition, since there is a through-hole below and deposition needs to be carried out on the sidewall of the deposition layer of path 3, excessive energy provided by path 4 could melt the deposition layer of path 3, resulting in the overall collapse of the deposition layer. As shown in Figure 5, the energy input of path 4 is the lowest. path 3 and path 4 have repaired all the small holes, but due to the repair holes being through-holes, there will be a certain depression in the deposition layer. Path 4 cannot provide more energy for filling, so path 5 is needed to provide more energy and fill more material to fill the remaining repair area. Path 6, on the other hand, is

aimed at improving the fluidity of the repair surface molten pool to ensure the forming quality of small hole repair.

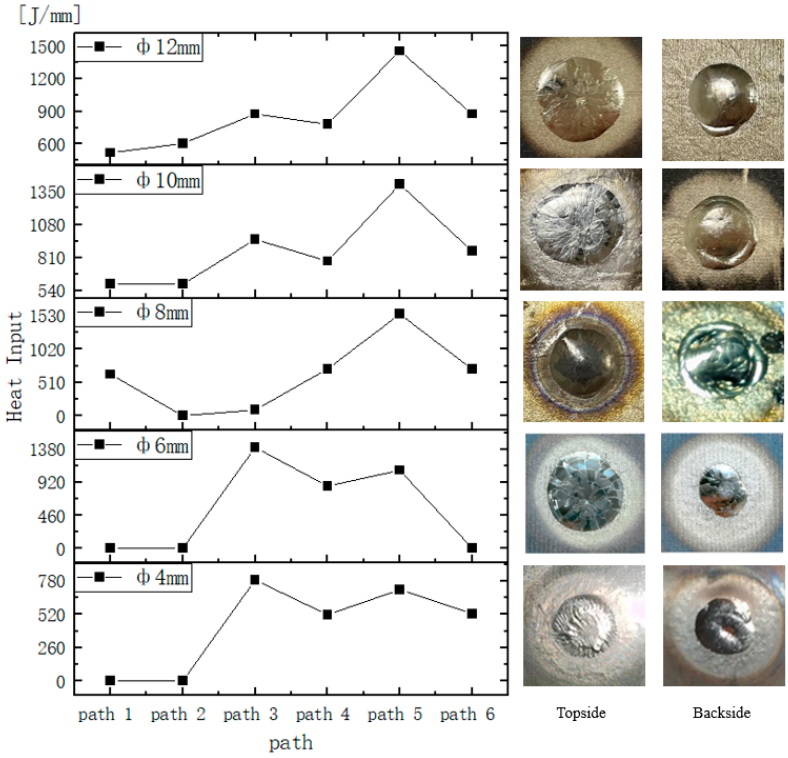


Figure 5. The influence of heat input on the forming of process holes.

In Figure 4c,d, path 1 and path 2 are designed to ensure that small holes of different diameters can all be repaired. Before repairing the small holes, a shrinking process is applied to them to ensure that path 3, path 4, and path 5 in Figure 4b can maintain the forming quality of small hole repair during the repair process.

As shown in Figure 4, images depict the repair and formation of small holes with different scales. Through the control of heat input zones and optimization of the repair path, a single-side welding and double-side forming process for the repair of through-holes in components with various aperture sizes was successfully achieved.

As shown in Figure 4, it illustrates the variations in heat input for different aperture sizes and different repair paths. Comparing the heat input between path 3 and path 5 for repairing small holes with apertures of φ4 mm and φ6 mm, it is evident that the heat input for the φ6 mm small hole repair process is significantly higher than that for the φ4 mm small hole repair process. This discrepancy is due to the larger diameters of the base hole and the top opening for the φ6 mm small hole, requiring more material to ensure the forming quality of the small hole repair. However, when the motion reaches path 6, the heat input for the φ6 mm aperture becomes 0. This occurs because the total heat input for the φ6 mm small hole is higher than that for the φ4 mm small hole, improving the flowability of the molten pool and ensuring better material filling, thus guaranteeing the forming quality of the small hole repair.

Analyzing the variation in heat input for different repair paths for an aperture size of φ8 mm reveals that when the small hole aperture is $\geq$φ8 mm, the base hole's diameter is too large, making it challenging to meet the repair requirements solely through the repair process. Therefore, performing diameter reduction repair on the base hole ensures that its diameter meets the process requirements for repairing the small hole. When examining the heat input variation curves for different paths of the φ8 mm aperture, it is evident that the heat input for path 3 is significantly lower than that for other aperture sizes. This reduction

in heat input is due to achieving both diameter reduction repair for the base hole with a φ8 mm aperture and simultaneous material filling in the repair region.

Through the analysis of the heat input variation curves for repair paths (path 1–path 2) for small holes with apertures of φ8 mm, φ10 mm, and φ12 mm, it was observed that the number of circles for repairing the base hole of apertures φ10 mm and φ12 mm exceeded that of the φ8 mm aperture. This is because, when the base hole diameter is ≥φ10 mm, a single-pass diameter reduction repair process is insufficient to meet the repair requirements. It becomes necessary to perform multiple layers and multiple passes of diameter reduction repair on the base hole before proceeding with the repair process.

4. The Mechanical Properties and Analysis of Microstructure

4.1. Detection of Overheight in the Repair Area

Measurements were taken on the front and backside residual heights of continuously repaired small holes, as depicted in Figure 3. As illustrated in Figure 6, measurements were conducted using a depth-of-field microscope, analyzing the two-dimensional and three-dimensional profiles of the highest point in the repair area. The height of the highest point was recorded at 0.64 mm. The maximum residual height within the repair area was also found to be 0.64 mm.

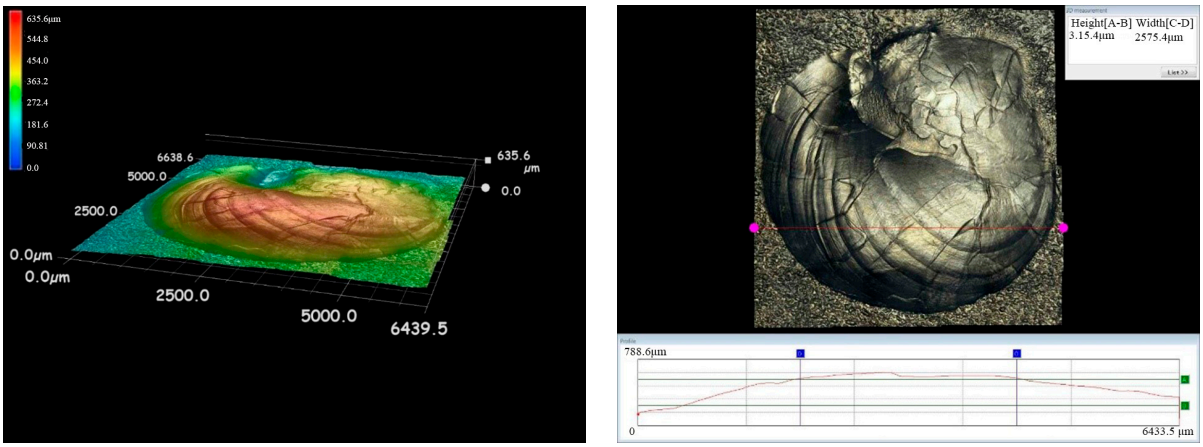


Figure 6. Ultra depth of field microscope detection.

Figure 7 demonstrates the measurements of the front and backside residual heights of the repaired small holes using metallographic inspection. Both front and backside residual heights within the repair area were controlled to be within 0.6 mm. After the repair, there is a smooth transition between the deposited layer on the backside and the substrate, minimizing the contact angle between them. This helps to avoid significant stress between the deposited layer and the substrate, preventing abrupt changes in height due to large contact angles, which can lead to fracture and detachment of the deposited layer during the operation of the aerospace engine casing.

Additionally, since it is impractical to modify the morphology of the backside during the repair of the boreholes in the aerospace engine casing, it is essential to control the positive and negative surface height differences on both the front and back sides after repair. This control is necessary to prevent issues such as localized mass increase in the repaired area due to excessive thickness of the deposited layer, leading to operational imbalance and potential local failure during the engine's operation. Meeting the repair requirements for aerospace engine casing, the machining height difference in the repaired area is kept below 1 mm, satisfying the dimensional requirements for borehole repair.

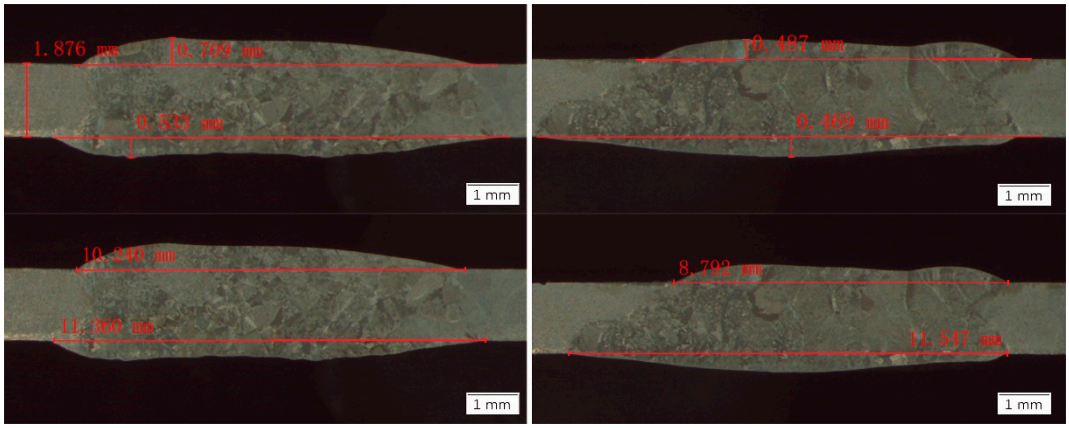


Figure 7. Measurement of front and back reinforcement in the repair area.

4.2. Tensile Performance Testing

As shown in Figure 8, using the repair area as the symmetric center, the welded specimens were subjected to tensile sample processing using the wire cutting method. Tensile strength measurements of the weld zone were conducted using an electronic universal material testing machine, with a strain gauge used to record the deformation process. The tensile testing rate was set at 1 mm/min. Prior to testing, the tensile specimens were surface-polished to remove any wire cutting marks. Subsequently, specimen 4 was clamped onto the electronic universal material testing machine for measurement. The obtained results are as follows: In the red circles, as shown in Figure 8, the stretching fracture occurred within the weld seam area. The cracks adjacent to the fracture surface were caused by line cutting during fracture scanning. For the φ4 mm specimen, the tensile strength was 1069 MPa with an elongation of 13.8%. For the φ8 mm specimen, the tensile strength was 977 MPa with an elongation of 21.3%.For the φ10 mm joint, the joint strength was 978 MPa with an elongation of 15.9%. All fractures occurred at the weld seam, and the tensile strength of each specimen exceeded the base material's strength of 895 MPa. With an increase in repair hole diameter, both the forming quality and mechanical properties of the repair area showed a decreasing trend.

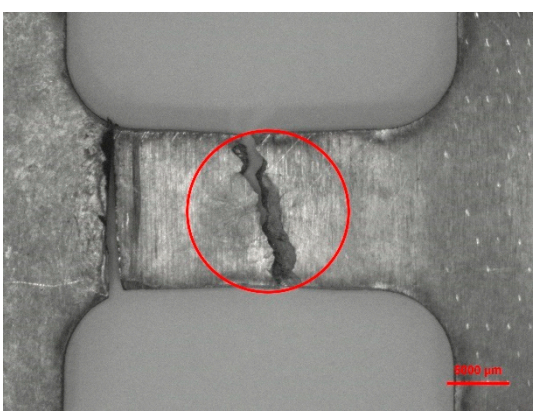
As shown in Figure 8, the fractures occurred consistently at the weld seam, and the tensile strength significantly exceeded that of the base material, which was 895 MPa. This is attributed to the repair process, where a portion of the repaired material is heated to high temperatures, melted, and gradually cooled. Essentially, it subjects the repaired material to a heat treatment process, significantly impacting the size and mechanical properties of the heat-affected zone. As the repair path progresses, the size of the heat-affected zone gradually increases.

4.3. Metallographic Microstructure and Hardness Analysis

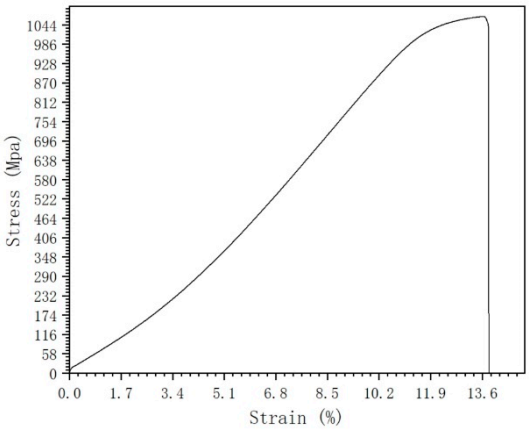
As shown in Figure 9(4), the ZTC4 titanium alloy, as a common cast $\alpha + \beta$ titanium alloy, consists of lamellar α phase and intergranular β phase in the cast state. Comparing Figure 9(4) with Figure 9(2), it can be observed that the grain size in the deposited layer region is smaller than that of the base material, exhibiting better comprehensiveness. Furthermore, by comparing Figure 9(4) with Figure 9(2) as well as Figure 9(1,3), it is evident that although the grain size in the heat-affected zone is larger than that in the deposited layer, the grains in the heat-affected zone show characteristics of equiaxed grains, with dimensions slightly smaller than those of the base material. The deposited layer exhibits a dense structure, with no apparent defects such as cracks or pores on its surface and interior.

Through Vickers hardness testing, as shown in Figure 10, the hardness in the repair zone is 480 HV, higher than the base material hardness of 380 HV. The organizational performance in the repair zone surpasses that of the base material. However, the hardness curve in the heat-affected zone exhibits a decreasing trend from the repair zone to the

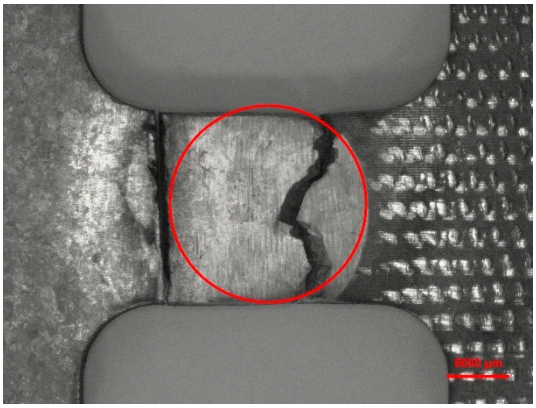
base material region. Nevertheless, the average hardness remains higher than that of the base material.



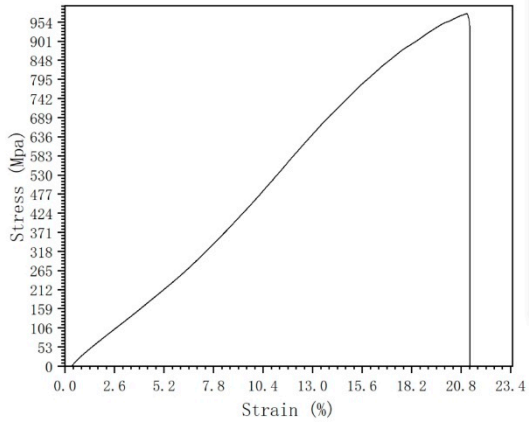
(**a**) Φ4 test specimen



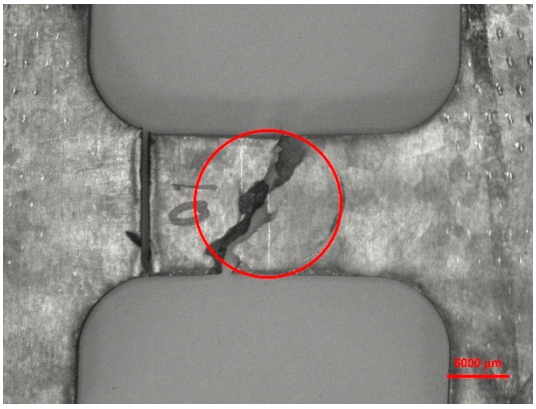
(**b**) The stress–strain curve of Φ4



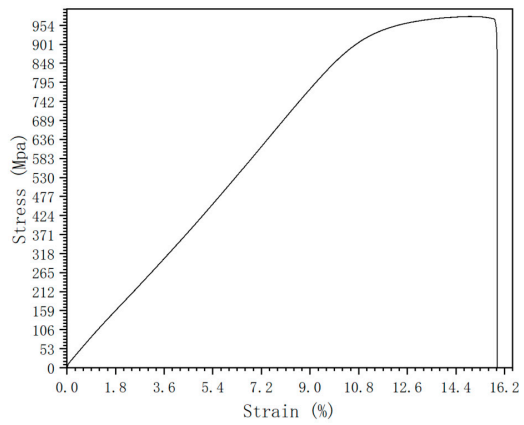
(**c**) Φ8 test specimen



(**d**) The stress–strain curve of Φ8



(**e**) Φ10 test specimen



(**f**) The stress–strain curve of Φ10

Figure 8. Tensile performance test.

This is attributed to the influence of the droplet transfer trajectory. The repair zone is affected by multiple heat inputs, leading to a significant increase in the needle-like α-martensite with high hardness. In contrast, the base material and heat-affected zone experience less influence from multiple heat inputs, resulting in less pronounced changes in the organizational structure influenced by the droplet transfer trajectory. Therefore, the droplet transfer trajectory contributes to the higher hardness in the repair zone compared

to the heat-affected zone and base material, with a noticeably increased size of the high-hardness zone.

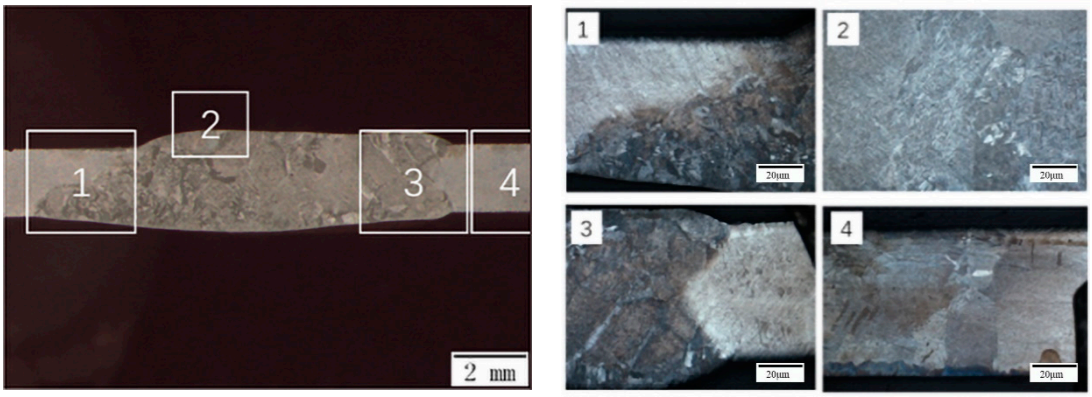


Figure 9. Analysis of repair area and heat-affected area.

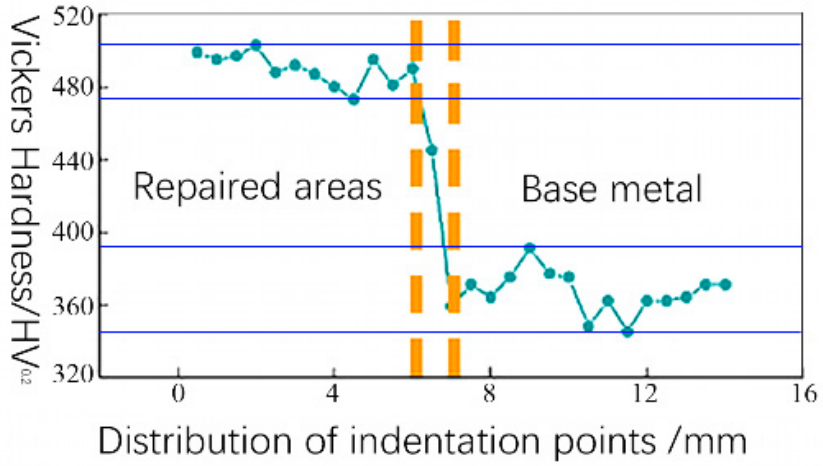


Figure 10. Hardness analysis.

5. Conclusions

(a) By controlling the frequency and amplitude of wire vibration feeding, it is possible to effectively control the size of the droplet transition. Further control of the direction of droplet entry into the molten pool enables the directional transition of droplets during the repair process of through-hole defects.

(b) Through a comparative analysis of the droplet detachment behavior at different frequencies of wire vibration feeding, it was found that at f = 3 Hz, a stable intermittent liquid bridge transition can be achieved.

(c) The weld reinforcement of the engine casing machining holes is less than or equal to 0.7 mm. The weld beads have a 100% first-pass qualification rate by X-ray and fluorescence penetration testing. The repair area hardness reaches 480 HV, and the tensile strength reaches 1069 MPa. The mechanical properties meet the repair process requirements for aerospace engine casings.

(d) Compared to repair methods such as HOVE and PASW laser cladding, which utilize powder as the deposition layer material, and the traditional TIG repair method, the repair method mentioned in this paper shows no occurrence of pores. The tensile strength and elongation reach 1069 MPa and 13.8%, respectively, with a hardness of 480 HV. In all performance aspects, it outperforms the aforementioned methods while also avoiding secondary pollution to the interior of aerospace engine casings caused by powder materials.

(e) Through partitioned control of heat input and optimized matching of repair paths, automated repair of through-hole components without protection on the backside has been achieved, along with single-side welding and double-side forming control during the repair process of components with different diameters of holes. Compared to traditional manual repair methods, the repair method mentioned in this paper exhibits significantly higher efficiency and forming quality.

Author Contributions: Conceptualization, Y.P. and H.L.; Methodology, S.G.; Validation, S.G.; Formal analysis, Y.P., W.Z. and Y.M.; Investigation, Y.P. and W.Z.; Resources, Y.P. and Y.M.; Data curation, S.G.; Writing—original draft, Y.P.; Writing—review and editing, H.L., W.Z. and Y.M.; Supervision, H.L. All authors have read and agreed to the published version of the manuscript.

Funding: This research was funded by the key research and development program of Heilongjiang Province (No. GA21A401) and the National Key Research and Development Program (No. 2022YFC3005900).

Data Availability Statement: The data presented in this study are available on request from the corresponding author. The data are not publicly available due to privacy.

Conflicts of Interest: The authors declare no conflict of interest.

References

1. Srinivasan, D. Challenges in Qualifying Additive Manufacturing for Turbine Components: A Review. *Trans. Indian Inst. Met.* **2021**, *74*, 1107–1128. [CrossRef]
2. Bermingham, M.; St John, D.H.; Krynen, J.; Tedman-Jones, S.; Dargusch, M. Promoting the columnar to equiaxed transition and grain refinement of titanium alloys during additive manufacturing. *Acta Mater.* **2019**, *168*, 261–274. [CrossRef]
3. Angel, N.M.; Basak, A. On the fabrication of metallic single crystal turbine blades with a commentary on repair via additive manufacturing. *J. Manuf. Mater. Process.* **2020**, *4*, 101. [CrossRef]
4. Tian, L.I.; Zhou, D.W.; You-rui-ling, Y.A.N.; Ping, P.E.N.G.; Liu, J.S. First-principles and Experimental Investigations on Ductility/Brittleness of Intermetallic 121 Compounds and Joint Properties in Steel/Aluminum Laser Welding. *Trans. Nonferrous Met. Soc. China* **2021**, *31*, 2962–2977.
5. Cui, S.; Shi, Y.; Sun, K.; Gu, S. Microstructure evolution and mechanical properties of keyhole deep penetration TIG welds of S32101 duplex stainless steel. *Mater. Sci. Eng. A* **2018**, *709*, 214–222. [CrossRef]
6. Saboori, A.; Aversa, A.; Marchese, G.; Biamino, S.; Lombardi, M.; Fino, P. Application of directed energy deposition-based additive manufacturing in repair. *Appl. Sci.* **2019**, *9*, 3316. [CrossRef]
7. Cao, Y.; Wei, H.; Yang, T.; Liu, T.; Liao, W. Printability assessment with porosity and solidification cracking susceptibilities for a high strength aluminum alloy during laser powder bed fusion. *Addit. Manuf.* **2021**, *46*, 102103. [CrossRef]
8. Cunningham, C.; Flynn, J.; Shokrani, A.; Dhokia, V.; Newman, S. Invited review article: Strategies and processes for high quality wire arc additive manufacturing. *Addit. Manuf.* **2018**, *22*, 672–686. [CrossRef]
9. Balasubramanian, V.; Ravisankar, V.; Reddy, G.M. Effect of pulsed current and post weld aging treatment on tensile properties of argon arc welded high strength aluminium alloy. *Mater. Sci. Eng. A* **2007**, *459*, 19–34. [CrossRef]
10. Chen, X.; Lei, Z.L.; Chen, Y.B.; Jiang, M.; Jiang, N.; Bi, J.; Lin, S.B. Enhanced wetting behavior using femtosecond laser-textured surface in laser welding brazing of Ti/Al butt joint. *Opt. Laser Technol.* **2021**, *142*, 107212. [CrossRef]
11. Liu, C.; Zhang, C.; Du, P. Study on Supersonic Flame Spray Protective Coating and Its Tribological Properties on TC4 Titanium Alloy Surface [J/OL]. Surface Technology: 1–12. Available online: https://kns-cnki-net.webvpn.nepu.edu.cn/kcms/detail/50.1083.tg.20230619.1436.002.html (accessed on 5 March 2024).
12. Okawa, T.; Shimanuki, H.; Funatsu, Y.; Nose, T.; Sumi, Y. Effect of preload and stress ratio on fatigue strength of welded joints improved by ultrasonic impact treatment. *Weld World* **2013**, *57*, 235–241. [CrossRef]
13. Wei, Z.; Li, G.; Wang, Y. The microstructure and properties of TC4 titanium alloy manufactured by TIG arc additive manufacturing. *Nonferrous Met. Eng.* **2021**, *11*, 14–19+63.
14. Shan, Q.; Chen, L.; Jing, Y.; Zhan, Y.; Liu, C. The effect of scanning strategy on the microstructure, properties, and residual stress of laser melted deposited TC4 titanium alloy. *Prog. Laser Optoelectron.* **2021**, *58*, 256–264.
15. Guo, W.; Sun, R.; Song, B.; Zhu, Y.; Li, F.; Che, Z.; Li, B.; Guo, C.; Liu, L.; Peng, P. Laser shock peening of laser additive manufactured Ti6Al4V titanium alloy. *Surf. Coat. Technol.* **2018**, *349*, 503–510. [CrossRef]
16. Owoseni, T.A.; Ciudad de Lara, I.; Mathiyalagan, S.; Björklund, S.; Joshi, S. Microstructure and Tribological Performance of HVAF-Sprayed Ti-6Al-4V Coatings. *Coatings* **2023**, *13*, 1952. [CrossRef]
17. Wei, W.; Guangfu, C.; Hongming, G. Analysis of microstructure transformation and mechanical properties of TC4 alloy TIG welded joints. *J. Weld.* **2009**, *30*, 81–84.

18. Hu, L.; Huang, J.; Zhuang, K.; Zhao, F.; Wu, Y. Influence of distance between laser and MIG arc on drop transfer process of CO_2 laser-MIG hybrid welding. *Trans. China Weld. Inst.* **2010**, *31*, 49–53.
19. Li, K.H.; Wu, C.S. Mechanism of metal transfer in DE-GMAW. *J. Mater. Sci. Technol.* **2009**, *25*, 415–418.
20. Shu, X. Research on the Manufacturing Method and TC4 Deposition Mechanism of Pre Melting Electron Beam Additives. Ph.D. Dissertation, Harbin Institute of Technology, Harbin, China, 2021.
21. Montalbano, T.; Briggs, B.N.; Waterman, J.L.; Nimer, S.; Peitsch, C.; Sopcisak, J.; Trigg, D.; Storck, S. Uncovering the coupled impact of defect morphology and microstructure on the tensile behavior of Ti-6Al-4V fabricated via laser powder bed fusion. *J. Mater. Process. Technol.* **2021**, *294*, 117113. [CrossRef]
22. Xian, G.; Oh, J.M.; Lee, J.; Cho, S.M.; Yeom, J.T.; Choi, Y.; Kang, N. Effect of heat input on microstructure and mechanical property of wire-arc additive manufactured Ti-6Al-4V alloy. *Weld. World* **2022**, *66*, 847–861. [CrossRef]
23. Sen, M.; Kurt, M. Laser and TIG welding of additive manufactured Ti-6Al-4V parts. *Mater. Test.* **2022**, *64*, 656–666. [CrossRef]
24. Sen, M.; Kurt, M. Comparison between laser and TIG welding of electron beam melted Ti6Al4V parts. *Mater. Test.* **2023**, *65*, 1776–1785. [CrossRef]

Disclaimer/Publisher's Note: The statements, opinions and data contained in all publications are solely those of the individual author(s) and contributor(s) and not of MDPI and/or the editor(s). MDPI and/or the editor(s) disclaim responsibility for any injury to people or property resulting from any ideas, methods, instructions or products referred to in the content.